CHARACTERIZATION OF WOVEN COMPOSITE MATERIAL UNDER MULTIAXIAL LOADING REGIMES USING FE-BASED STEREOCORRELATION

Andrija Zaplatić[a,b], Zvonimir Tomičević[a,*], François Hild[b]

[a] *University of Zagreb, Faculty of Mechanical Engineering and Naval Architecture, 10002 Zagreb, Croatia*

[b] *Université Paris-Saclay, CentraleSupélec, ENS Paris-Saclay, CNRS, LMPS – Laboratoire de Mécanique Paris-Saclay, 91190 Gif-sur-Yvette, France*

* corresponding author: zvonimir.tomicevic@fsb.unizg.hr

ABSTRACT. In this paper, woven glass fiber composite samples were subjected to three different cyclic loading histories (i.e., tensile, shear and combined loading at 45° via the Modified Arcan Fixture. During the experiments, the samples were monitored by a stereovision system. Finite Element based stereocorrelation was used to measure the displacement and strain fields. The analysis of the experiments revealed different damage mechanisms. Furthermore, for the 45° experiment, the highest strain levels were reached, whereas for the tensile test, the highest stress levels were achieved.

KEYWORDS: Stereocorrelation, woven composite, Arcan fixture, multiaxial loading.

1. INTRODUCTION

The mechanical characterization of various materials is essential for designing and optimizing engineering components. In modern engineering, traditional materials like steel and alloys are increasingly being replaced by fiber-reinforced polymer (FRP) composites [1]. These composites are highly sought after for their excellent strength-to-weight ratio. An additional advantage of FRPs is their customizable architecture, which can be tailored to meet specific workload conditions. However, predicting the ultimate failure and degradation of these components remains challenging due to their complex architecture. Predicting their lifetime is also challenging due to their heterogeneity, which makes composites susceptible to various damage mechanisms that may degrade their stability [2]. Therefore, extensive experimental investigations are necessary to study the composite behavior under different loading regimes [3]. Since uniaxial mechanical tests do not adequately simulate real-world conditions, more complex loading configurations are required. However, these tests often demand high-cost and specialized testing machines, which may not be readily available.

To address this issue, specially designed loading apparatuses for uniaxial testing machines have been developed. One popular setup is the Modified Arcan Fixture (MAF) [4–6], which applies three distinct loading regimes (i.e., tensile, shear, and their varied combinations at several angles) to butterfly-shaped specimens. The MAF allows for testing a variety of materials, including wood [7] and composite joints [8], although it was originally designed for composite materials [9].

Due to the complex geometry of the Arcan samples, which features two V-notches in the ligament area, classical contact measurement equipment is highly impractical. As a result, contactless optical measurement methods like Digital Image Correlation (DIC) are more suited [10, 11]. DIC utilizes visible light cameras to perform full-field measurements, and in recent years, the global DIC approach has gained popularity [12]. This approach incorporates Finite Element (FE) features in such a way that displacement measurements are performed on meshes. Consequently, the resulting outputs are nodal displacements, from which strain fields are determined. Additionally, this method provides correlation residuals, which highlight damaged areas during the experiment [13]. An added advantage of FE-based approaches is the continuity assumption of the displacement fields, eliminating the need for interpolation as required in local approaches [14].

If out-of-plane motions are expected or a complex 3D sample is being tested, multiple cameras are employed within a stereovision framework [15, 16]. The finite element method has also been integrated into stereocorrelation environments [17–19]. By utilizing the known FE geometry of the observed object, it is possible to perform camera calibration directly on the object itself [19, 20] and then measure 3D surface displacements.

2. MATERIALS AND METHODS

In this section, the woven composite samples, experimental setup, and investigation are presented. Additionally, the FE-based stereocorrelation method is briefly introduced.

2.1. MATERIAL

The investigated composite samples were manufactured by reinforcing a vinylester resin with woven glass fibers. The 3 mm thick samples were composed
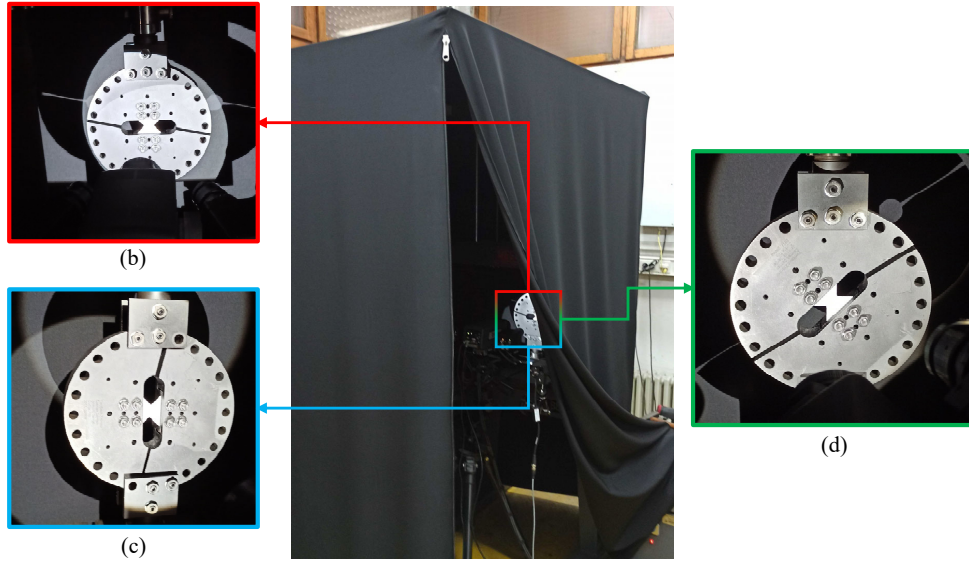
FIGURE 1. Experimental setup. (a) Testing machine and optical system protected by black fabric. Loading configurations: (b) tension, (c) shear and (d) combined tension and shear at 45°.

of 7 layers of woven fabric, where the yarns were 0°/90° oriented. Additionally, the fabric layers were stacked identically on top of each other.

Due to the complex geometry of the samples and the use of glass fibers, conventional machining methods were sub-optimal for processing the composite plates. Therefore, water jet technology was used to cut the samples from the composite plates. To ensure sample failure during the experiment, two additional V-notches were cut for each sample. These additional notches were 2 mm long and 0.5 mm wide, thereby reducing the net section area to approximately $48\,\mathrm{mm}^2$.

2.2. Experimental investigation

The experimental setup (Figure 1a) consisted of the MAF and the optical system. The MAF allows for different loading conditions to be applied to the Arcan sample by rotating the fixture relative to the loading axis. In this research, three Arcan specimens were tested and three loading configurations were prescribed, namely tension (WF00) (Figure 1b), shear (WF90) (Figure 1c), and their combination at 45° (WF45) (Figure 1d). For each experiment, the sample was loaded at a velocity of $2\,\mu\mathrm{m\,s}^{-1}$ in displacement control mode on the Messphysik Beta 50-5 uniaxial testing machine, each experiment consisting of eight loading/unloading cycles. The testing speed was chosen according to previous research [13, 20]. The samples were intermittently taken out of the MAF to perform X-ray computed tomography scanning to obtain any micro-structural changes inside of the material. Therefore, cyclic loading regimes were defined.

To minimize external lighting influences that could affect brightness and contrast conditions, the experimental and optical setups were covered with black fabric (Figure 1a). The optical system included two identical visible light cameras that monitored the surfaces of the samples during the experiments. Furthermore, two light sources were employed to illuminate the sample surface.

2.3. FE based stereocorrelation

In this work, FE-based stereocorrelation [5, 21] was performed to measure 3D surface displacement fields using FE meshes [17–19], which correspond to the observed sample geometry. Additionally, strain fields were calculated from the measured displacement fields.

Stereocorrelation consists of two main steps, namely, calibration and correlation. In the calibration step, the projection matrix $[\pi]$ for each camera is determined, allowing the FE mesh to be projected onto both camera images, defining the same Region of Interest (ROI). The projection matrix $[\pi]$ can be built if the intrinsic and extrinsic camera parameters are known. However, usually they are unknown and are determined with the calibration. The calibration can be defined as a least square minimization between the two camera images

$$\rho^2(\{\mathbf{P}\}) = \sum_{ROI} \|f_1(\mathbf{x}_1) - f_2(\mathbf{x}_2)\|^2, \qquad (1)$$

where $\{\mathbf{P}\}$ is a vector that gathers all the sought intrinsic and extrinsic parameters, $\mathbf{x}_c$ are the projected physical points defined over the FE mesh $\mathbf{X}$

$$\mathbf{x}_c = \mathbf{x}_c(\mathbf{X}, [\pi_c]). \qquad (2)$$

In the correlation step, the nodal-wise displacement field $\mathbf{U}(\mathbf{X}, t)$ is measured for any given time-step t. The new cost function can be written as

$$\mathbf{U}(\mathbf{X}, t) = \arg\min \sum_{c=1}^{N_c} \sum_{ROI} (\tilde{g}_c(\mathbf{x}_c, t) - f_c(\mathbf{x}_c))^2, \quad (3)$$

where f_c are the respective camera reference images, $\tilde{g}_c$ the corrected deformed image at time t by the kinematic field $\mathbf{U}(\mathbf{X}, t)$ for each respective camera and N_c is the camera number. The regularity of the kinematic field $\mathbf{U}(\mathbf{X}, t)$ in space is ensured by using a set of spatial shape functions $\psi_i(\mathbf{X})$

$$\mathbf{U}(\mathbf{X}, t) = \sum_{i=1}^{DOF} u_i(t)\boldsymbol{\psi}_i(\mathbf{X}), \qquad (4)$$

where DOF is the number of degrees of freedom, $u_i(t)$ are the nodal displacements for the time t. In these analyses, the FE meshes consisted of three-noded elements (T3) [19]. Furthermore, the camera-wise gray level residuals ϕ_c can be computed for each physical point x_c

$$\phi_c = \tilde{g}_c \left(\mathbf{x}_c, t \right) - f_c \left(\mathbf{x}_c \right). \qquad (5)$$

Both the calibration and correlation are performed by resorting to the iterative Gauss-Newton scheme. For more detailed information, the reader is referred to Zaplatić et al. [20], Chang et al. [16, 21].

3. Results

In this section, the stereocorrelation results are presented for all three experiments. The major principal strain (Figure 2) and stereocorrelation residual (Figure 3) fields are displayed for the maximum achieved stress level σ_{max} for each experiment respectively (Table 1). From Table 1, it is concluded that the highest stress level was achieved for the tensile test (WF00), whereas the lowest was reached for the shear test (WF90).

In Figure 2 the major principal strain fields are displayed for all three experiments for the maximum stress levels (Table 1). First, for the tensile test (Figure 2a), two concentrated strained bands emanating from the notches are observed. Furthermore, four additional strain concentrations are distinguished on the peripheral areas of the sample. Since the yarns were parallel to the tensile load, the middle part was the most rigid part of the sample, whereas the peripheral areas were not. Hence, they were more prone to damage.

In the shear experiment (Figure 2b), a single strained band is visible in the gauge region, parallel to the loading direction. At the roots of the notches, the strain levels were the highest, whereas the top and bottom parts exhibited very small strain values.

For the WF45 experiment, a single strained band developed between the V notches (Figure 2c), similarly to WF90 test. However, it was slightly inclined compared to the WF90 strained band. Two strain concentrations are visible at diagonal peripheral areas of the sample, depicted by the green circles.

Using the stereocorrelation residuals, it is possible to reveal if surface damage developed. For the tensile test (Figure 3a), three cracks formed around the root of the left notch. Four cracks also developed in peripheral areas, which were also visible in
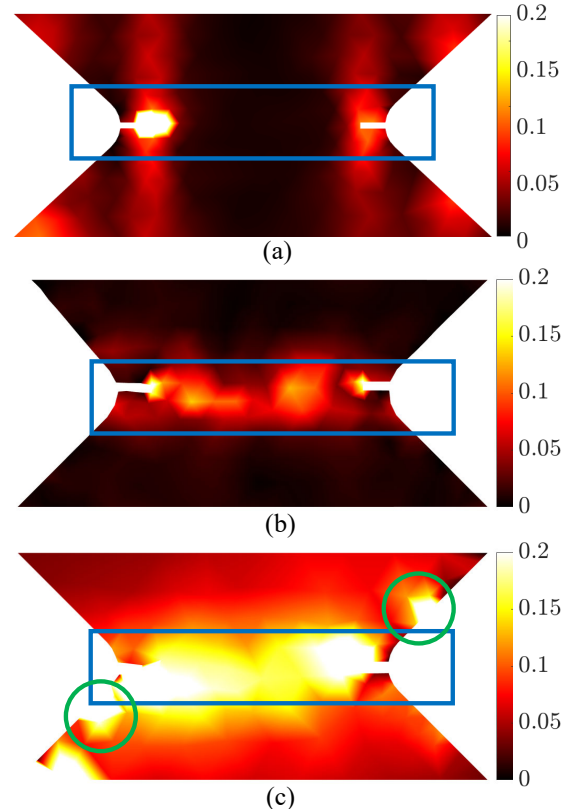

FIGURE 2. Major principal strain fields for (a) test WF00, (b) test WF90 and (c) test WF45 at the ultimate stress. The blue squares depict the virtual gauges where the nodal strain values were extracted and averaged. The green circles highlight strain concentrations outside of the virtual gauge.

Experiment	σ_{max}
WF00	300 MPa
WF90	78 MPa
WF45	178 MPa

TABLE 1. Ultimate stress levels for each experiment.

the corresponding strain field (Figure 2a). Several small horizontal cracks are observed on the surface of the sample, which corresponded to surface matrix cracks [20].

In the residual field of the shear experiment (Figure 3b), a major crack is distinguished, which emanated from the root of the left notch. The entire gauge region displayed increased residuals, which further indicated damage on the surface.

Last, for the 45° experiment, increased residuals are present across the entire middle gauge region of the sample (Figure 3c). The residual levels are higher than in the previous two experiments (Figure 3a, b). Similarly to the strain field, increased residuals spread out diagonally on the opposite ends of the gauge area.
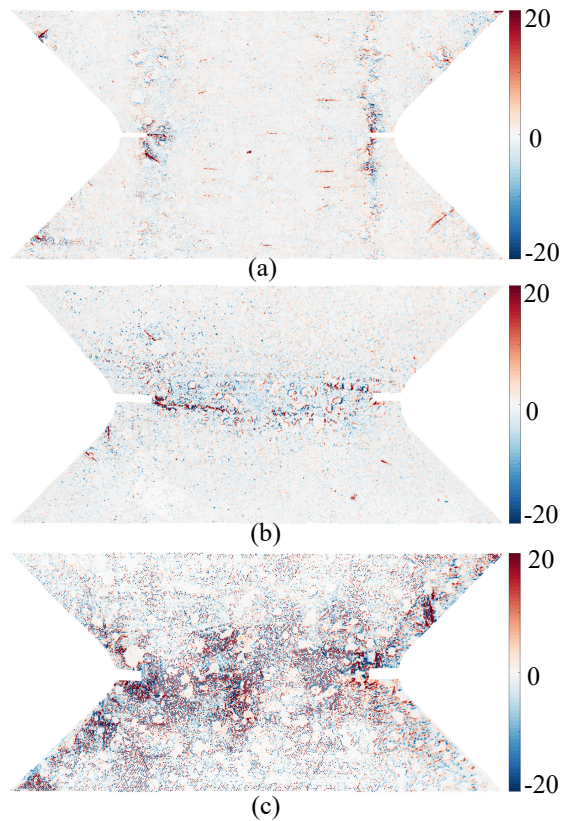
FIGURE 3. Stereocorrelation residual fields for (a) WF00, (b) WF90 and (c) WF45 tests for the ultimate stress. The residuals are expressed as a percentage of the dynamic range of the camera reference images.

FIGURE 4. Stress-major principal strain curves for all three experiments.

4. DISCUSSION

In this section, the stress-strain responses (Figure 4) of the three experiments are compared and discussed. The stresses were calculated as the applied force divided by the net section area of each sample. The average strain levels were determined from virtual strain gauges defined for each experiment in Figure 2.

As previously noted, the tensile test exhibited the highest stress levels, while the shear experiment showed the lowest. When examining the stress-strain curves, it is observed that the tensile test resulted in the lowest strain levels, whereas the combined tensile and shear experiment achieved the highest strain levels. This difference is attributed to the orientation of yarns with respect to the loading direction. The tensile test corresponded to the highest rigidity due to the aligned yarn orientation, whereas shear exhibited the lowest rigidity. The WF45 experiment had yarns oriented at 45° with respect to the loading direction; thus it had increased rigidity compared to the shear experiment.

5. CONCLUSION

In this work, FE based stereocorrelation was applied to characterize the mechanical response and behavior of woven glass fiber composite samples under three distinct loading configurations. The main conclusion are as follows:
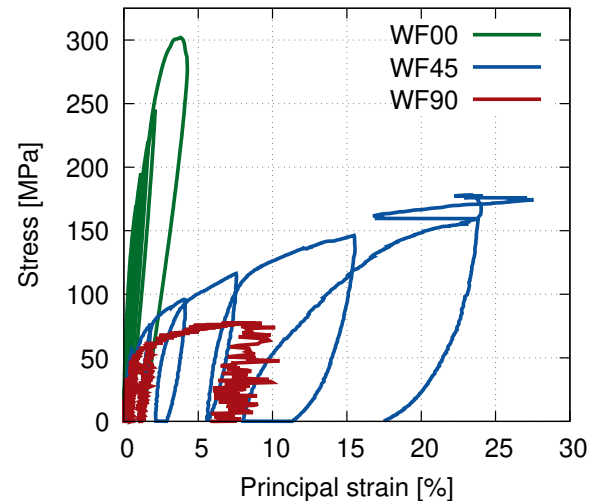
- The sample orientation with respect to the loading direction had a major influence on the stress-strain response, in particular its rigidity.

- The tensile test reached the highest stress level, whereas the shear experiment achieved the lowest.

- The highest strain and stereocorrelation residual levels were reached for the 45° experiment, thereby indicating the most accumulated damage on the investigated surfaces.

The experimental setup presented herein is not limited to composite materials. It was designed to be robust and versatile. Since the experimental protocol was established for different loading regimes, it is possible to introduce additional modalities in the stereocorrelation procedure, such as infrared and X-ray spectra for a more comprehensive material characterization.

REFERENCES

[1] R. Hsissou, R. Seghiri, Z. Benzekri, et al. Polymer composite materials: A comprehensive review. *Composite Structures* **262**:113640, 2021. https://doi.org/10.1016/j.compstruct.2021.113640

[2] A. Vrgoč, Z. Tomičević, B. Smaniotto, F. Hild. Application of different imaging techniques for the characterization of damage in fiber reinforced polymer. *Composites Part A: Applied Science and Manufacturing* **150**:106576, 2021. https://doi.org/10.1016/j.compositesa.2021.106576

[3] Q. Guo, Y. Zhang, D. Li, et al. Experimental characterization of the compressive properties and failure mechanism of novel multiaxial 3D woven composites. *Composites Communications* **28**:100905, 2021. https://doi.org/10.1016/j.coco.2021.100905

[4] M. Arcan, Z. Hashin, A. Voloshin. A method to produce uniform plane-stress states with applications to fiber-reinforced materials. *Experimental Mechanics* **18**(4):141–146, 1978. https://doi.org/10.1007/BF02324146

[5] A. Zaplatić, Z. Tomičević, D. Čakmak, F. Hild. Improvement of the Arcan setup for the investigation of thin sheet behavior under shear loading. *Experimental Mechanics* **62**(2):313–332, 2022. https://doi.org/10.1007/s11340-021-00762-1

[6] A. Zaplatić, A. Vrgoč, Z. Tomičević, F. Hild. Boundary condition effect on the evaluation of stress triaxiality fields. *International Journal of Mechanical Sciences* **246**:108127, 2023. https://doi.org/10.1016/j.ijmecsci.2023.108127

[7] J. Xavier, M. Oliveira, J. Morais, T. Pinto. Measurement of the shear properties of clear wood by the Arcan test. *Holzforschung* **63**(2):217–225, 2009. https://doi.org/10.1515/HF.2009.034

[8] A. Benelli, R. Ciardiello, C. B. Niutta, L. Goglio. Experimental and numerical characterization of adhesive joints with composite substrates by means of the Arcan test. *International Journal of Adhesion and Adhesives* **122**:103321, 2023. https://doi.org/10.1016/j.ijadhadh.2022.103321

[9] T. Laux, K. W. Gan, J. M. Dulieu-Barton, O. T. Thomsen. A simple nonlinear constitutive model based on non-associative plasticity for UD composites: Development and calibration using a Modified Arcan Fixture. *International Journal of Solids and Structures* **162**:135–147, 2019. https://doi.org/10.1016/j.ijsolstr.2018.12.004

[10] G. Besnard, H. Leclerc, F. Hild, et al. Analysis of image series through global digital image correlation. *Journal of Strain Analysis for Engineering Design* **47**(4):214–228, 2012. https://doi.org/10.1177/0309324712441435

[11] F. Hild, A. Bouterf, S. Roux. Damage measurements via DIC. *International Journal of Fracture* **191**(1-2):77–105, 2015. https://doi.org/10.1007/s10704-015-0004-7

[12] A. Zaplatić, Z. Tomičević, D. Čakmak, F. Hild. Identifiability of Ludwik's law parameters depending on the sample geometry via inverse identification procedure. *Coupled Systems Mechanics* **11**(2):133–149, 2022. https://doi.org/10.12989/csm.2022.11.2.133

[13] A. Vrgoč, Z. Tomičević, A. Zaplatić, F. Hild. Damage analysis in glass fibre reinforced epoxy resin via digital image correlation. *Transactions of FAMENA* **45**(2):1–12, 2021. https://doi.org/10.21278/TOF.452024020

[14] F. Hild, S. Roux. Comparison of local and global approaches to digital image correlation. *Experimental Mechanics* **52**(9):1503–1519, 2012. https://doi.org/10.1007/s11340-012-9603-7

[15] R. Fouque, R. Bouclier, J.-C. Passieux, J.-N. Périé. Stereo digital image correlation: formulations and perspectives. *Comptes Rendus Mécanique* **349**(3):453–463, 2021. https://doi.org/10.5802/crmeca.93

[16] X. Chang, C. L. Gourriérec, L. Turpin, et al. Proper Generalized Decomposition stereocorrelation to measure kinematic fields for high speed impact on laminated glass. *Computer Methods in Applied Mechanics and Engineering* **415**:116217, 2023. https://doi.org/10.1016/j.cma.2023.116217

[17] L. Dubreuil, J.-E. Dufour, Y. Quinsat, F. Hild. Mesh-based shape measurements with stereocorrelation. principle and first results. *Experimental Mechanics* **56**:1231–1242, 2016. https://doi.org/10.1007/s11340-016-0158-x

[18] J.-E. Pierré, J.-C. Passieux, J.-N. Périé. Finite Element Stereo Digital Image Correlation: Framework and mechanical regularization. *Experimental mechanics* **57**:443–456, 2017. https://doi.org/10.1007/s11340-016-0246-y

[19] M. Berny, T. Archer, P. Beauchêne, et al. Displacement uncertainty quantifications in T3-stereocorrelation. *Experimental Mechanics* **61**(5):771–790, 2021. https://doi.org/10.1007/s11340-021-00690-0

[20] A. Zaplatić, Z. Tomičević, X. Chang, et al. Hybrid infrared-visible multiview correlation to study damage in a woven composite complex-shaped specimen. *Coupled Systems Mechanics* **12**(5):445–459, 2023. https://doi.org/10.12989/csm.2023.12.5.445

[21] X. Chang, C. L. Gourriérec, F. Hild, S. Roux. Brightness and contrast corrections for stereocorrelation. Global and instantaneous formulation with spatial regularization. *Mechanical Systems and Signal Processing* **208**:111057, 2024. https://doi.org/10.1016/j.ymssp.2023.111057